

Observation of Dicke cooperativity between strongly coupled phonons and crystal-field excitations in a rare-earth orthoferrite

Authors: Fangliang Wu^{1,2†}, Xiaoxuan Ma^{3,4†}, Zhongwei Zhang^{1,2}, Motoaki Bamba^{5,6}, Jian Sun^{1,2}, Yuan Wan^{7,8}, Shixun Cao^{3,9*}, Qi Zhang^{1,2*}

¹National Laboratory of Solid State Microstructures and Department of Physics, Nanjing University, Nanjing 210093, China

²Jiangsu Physical Science Research Center, Nanjing University, Nanjing 210093, China

³Materials Genome Institute and Institute for Quantum Science and Technology, Shanghai University, Shanghai 200444, China

⁴ School of Material Science and Engineering, Shanghai University, Shanghai 200444, China

⁵Department of Physics, Graduate School of Engineering Science, Yokohama National University, Yokohama 240-8501, Japan

⁶Institute for Multidisciplinary Sciences, Yokohama National University, Yokohama 240-8501, Japan

⁷Institute of Physics, Chinese Academy of Sciences, Beijing 100190, China

⁸University of Chinese Academy of Sciences, Beijing 100049, China

⁹ Shanghai Key Laboratory of High Temperature Superconductors, Shanghai University, Shanghai, 200444, China

[†]These authors contributed equally to this work.

*Correspondence to: zhangqi@nju.edu.cn and sxcao@shu.edu.cn

Main text

Collective interactions between localized electronic excitations and the crystal lattice are central to many emergent phenomena in materials, including ferroelectricity and quantum magnetism. Despite its importance, the scaling behavior of such cooperativity remains largely unexplored. Here, we report the direct observation of Dicke-type cooperativity arising from the coupled phonons and non-degenerate crystal-field transitions (CFE), namely a pseudo-Jahn-Teller effect¹, in the rare-earth orthoferrite, ErFeO₃. Using magneto-Raman spectroscopy, we uncover strongly coupled spin, lattice, and orbital excitations. By varying the temperature, we identify the phonon-CFE coupling strength scales as \sqrt{N} , where N represents the effective ground-state population, which is a hallmark of Dicke cooperativity. Our findings verified the cooperative nature of the interaction between local Jahn-Teller ions and long-range phonons, offering a pathway for tailoring electronic and vibrational properties of materials through population control.

Cooperative effects represent the emergent collective behaviors, driven by the synchronization of quantum states across a large ensemble. A seminal example of such cooperativity is the Dicke superradiant phase transition (SRPT)^{2,3}, where local atomic ensembles interact with a single-mode light field. This interaction induces a phase transition in the atoms, resulting in an intensity-enhanced macroscopic coherent emission of light, compared to the spontaneous radiation. In such systems, the light-matter coupling strength scales as \sqrt{N} , with N denoting the number of atoms^{4,5}. As one of the few solvable models in many-body systems, Dicke physics has garnered significant interest, including the bosonic or fermionic SRPT^{6,7}, the extended Dicke model^{8,9}, and explorations of Dicke cooperativity in magnetic systems^{5,10-12}.

Beyond light-matter systems, cooperativity also governs critical phenomena in condensed matter, specifically between electronic and lattice degrees of freedom. It includes the cooperative Jahn-Teller effect (JTE), which is characterized by the spontaneous splitting of degenerate electronic ground states and an associated lowering of lattice symmetry¹³. The related pseudo Jahn-Teller effect (PJTE) involves coupling between non-degenerate states, often resulting in a weaker effect, and does not necessarily lead to a structural phase transition¹. Theoretically, a coupled system of two-fold electronic states and one phonon, denoted as the $E \otimes \beta$ Jahn-Teller model, can be formally mapped onto the Dicke SRPT model¹⁴.

Despite the theoretical analogy, experimentally, whether Dicke-type cooperativity and its hallmark \sqrt{N} scaling law persist in real material (pseudo) JTE systems is currently unresolved. Real materials are inherently subject to decoherence effects—including thermal fluctuations and quasiparticle scattering—that can suppress collective behavior. While JTE and PJTE have been extensively observed^{1,15}, the direct measurement and verification of the scaling laws governing their cooperative coupling strength has not yet been achieved.

In this paper, we report the direct observation of Dicke-type cooperative PJTE in orthoferrite ErFeO_3 . By performing magneto-Raman spectroscopy on a *c*-cut single crystal, we uncover coupled spin, lattice, and orbital degrees of freedom, including magnon-crystal-field excitation (CFE) strong coupling and phonon-CFE strong coupling. The latter case exhibits a prominent spectral avoided crossing between one phonon and one CFE, and the hybridization gap exhibits a \sqrt{N} scaling relation, where N represents the effective ground-state population, evidencing the Dicke-type cooperativity. Note that the involved electronic states are non-degenerate and the

coupling induces no structural change, thus the observed Dicke cooperative is associated with the pseudo JTE.

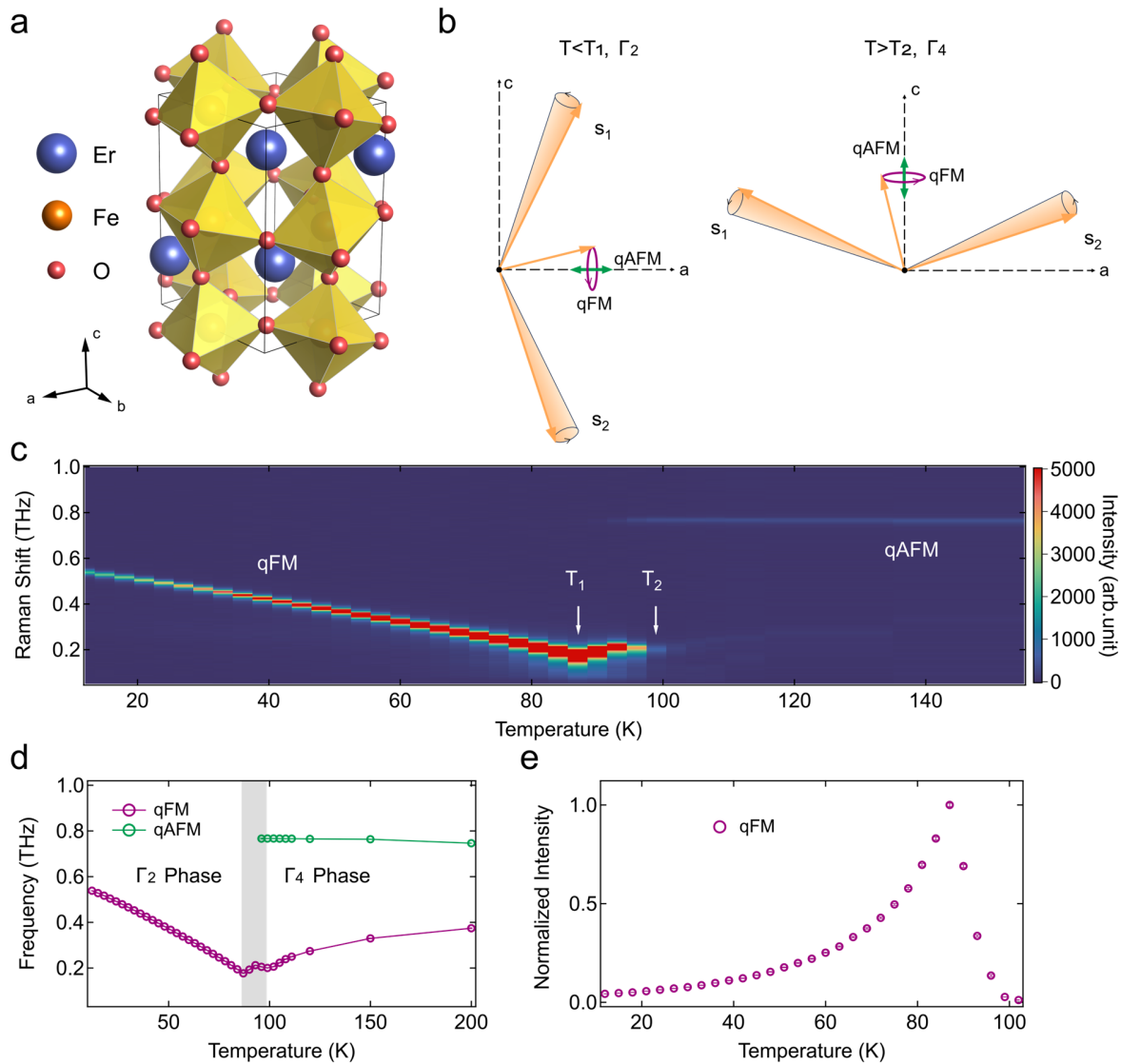


Figure 1 | Raman detection of acoustic magnons and spin reorientations in ErFeO_3 . **a**, the crystal structure of ErFeO_3 . **b**, Schematics of magnons and spin reorientation. The S_1 and S_2 denote spins of Fe^{3+} ions at neighboring sublattices. The magenta and green arrows indicate the two types of collective precession of the net magnetic moment associated with qFM and qAFM modes, respectively. **c**, Raman spectra of acoustic magnons as a function of temperature. Two frequency minima of the qFM mode are observed, and the corresponding temperatures are the lower (T_1) and upper (T_2) bounds of the spin reorientation range. **d**, **e**, The extracted peak position and intensity of qFM and qAFM as a function of temperatures. Error bars represent one standard deviation throughout the work.

ErFeO_3 belongs to the orthorhombic space group $Pbnm$, with a distorted perovskite-type structure, as shown in Fig. 1a. The Fe^{3+} ions form a canted antiferromagnetic order below 640 K, while the Néel temperature (T_N) of Er^{3+} is 4.5 K¹⁶. In addition, spins of Fe^{3+} ions will reorient in the ac -plane within an interval temperature range ($T_1 < T < T_2$), as illustrated in Fig. 1b. Recent advances reveal intriguing quantum phenomena in ErFeO_3 , such as the Dicke cooperativity in the magnetic system⁵, and the phonon-induced transient magnetization¹⁷, originated from the coupled different degrees of freedom. From an experimental perspective, Raman spectroscopy is sensitive to all spin, orbital, and lattice excitations. The electronic Raman transition of rare-earth ions has been theoretically proposed and experimentally verified¹⁸⁻²⁰; meanwhile, by leveraging spin-orbital coupling (SOC), spin excitations can also be detected via Raman processes²¹. In the following, we will present the Raman detection of low-lying magnons, CFEs, and phonons of ErFeO_3 , and the strong coupling among them.

A unit cell of ErFeO_3 contains four Fe^{3+} ions, corresponding to four magnon branches. Two of them are the acoustic magnons²², i.e., the quasi-ferromagnetic mode (qFM) and the quasi-antiferromagnetic mode (qAFM), respectively. These two modes are observed in Raman measurements, as shown in Fig. 1c. As the temperature increases, the qFM mode exhibits a redshift accompanied by an increase in intensity until the spin reorientation regime, then it almost disappears at the high temperature Γ_4 phase. In contrast, qAFM mode is only observed in the Γ_4 phase and remains unchanged as the temperature further increases. Two frequency minima of qFM mode have been observed, as shown in Fig. 1d, corresponding to the spin reorientation temperatures T_1 (87 K) and T_2 (99 K), respectively. In addition, the qFM mode exhibits an intensity enhancement near T_1 , which is due to the increased thermal population, as shown in Fig. 1e. It can also be viewed as the result of enhanced spin instability near the transition temperature²³.

The spin reorientation in ErFeO_3 stems from the temperature-varying magnetic anisotropy²⁴, which relies on the thermal population of Er^{3+} ions and inherently couples to the orbital excitations of the ground-state multiplet of Er^{3+} . Due to the non-centrosymmetric Er sublattice (site symmetry C_s), all dipolar optical transitions among the $^4\text{I}_{15/2}$ ground-state multiplet are allowed. These crystal-field excitations largely govern the optical properties of orthoferrites in the THz range²⁵⁻²⁸. In principle, the strong SOC and weak crystal-field interaction of Er^{3+} 4f electrons result in the hybridized Russell-Saunders states and the Stark splitting of ground-state $^4\text{I}_{15/2}$. Owing to the Er-

Fe exchange interaction, the Kramers degeneracy is removed at zero magnetic field. It can exhibit further splitting under finite magnetic fields via the Zeeman effect, as schematically shown in Fig. 2d. The orbital transitions within the $^4I_{15/2}$ multiplet cover the energy scale of both magnons and phonons, giving the chance of coupling between different elementary excitations.

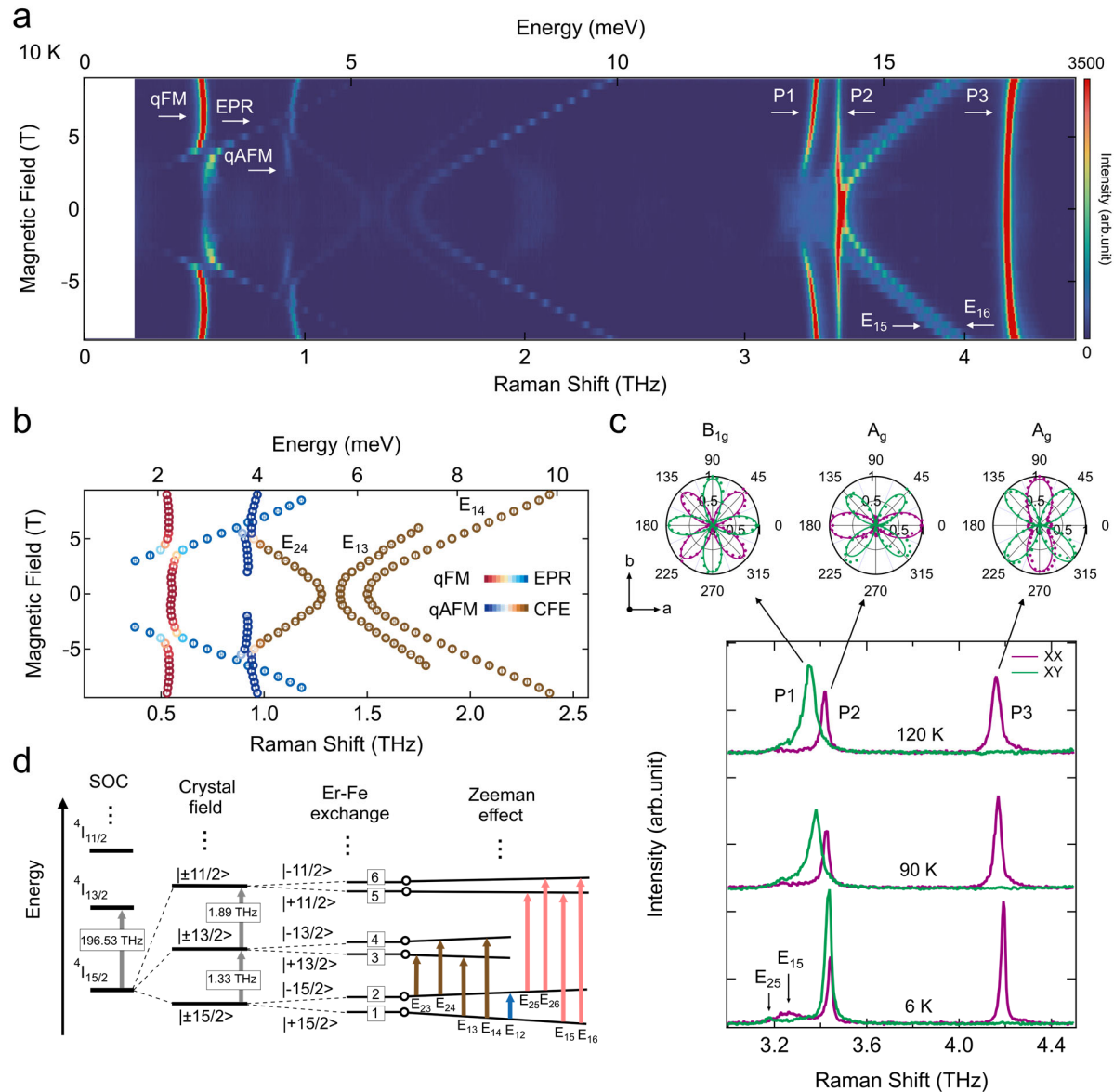


Figure 2 | Magneto-Raman spectra reveal coupled magnons, crystal-field excitations, and phonons in $ErFeO_3$. **a**, at 10 K, magneto-Raman spectra of *c*-cut $ErFeO_3$ from -9 to $+9$ T. EPR represents electronic paramagnetic resonance. **b**, the extracted peak positions of magnons and CFEs. The color of the data points indicates the proportion of different elementary excitations. **c**, polarization-resolved Raman spectra of P1, P2, and P3 phonons. The magenta and green lines represent the Raman spectra in the co- (XX) and cross- (XY) polarization channels. **d**, schematic diagrams of energy levels of the Er^{3+} ion.

By performing magneto-Raman spectroscopy on a *c*-cut ErFeO₃ crystal up to 9 T, multiple elementary excitations are observed below 4.5 THz, as presented in Fig. 2a. The qFM and qAFM modes are marked by white arrows. Although absent at zero field, the qAFM mode gradually emerges as the magnetic field increases. Besides magnons, the spin-flip CFEs between Kramers doublets $|\pm 15/2\rangle$ are observed with a *g*-factor of 5, which can be viewed as the electron paramagnetic resonance (EPR) of Er³⁺ ions. Crystal-field excitations between $|\pm 15/2\rangle$ and $|\pm 13/2\rangle$ also appear around 1.35 THz. As shown in Fig. 2d, there are four CFEs between two Stark energy levels, labeled as E₂₃, E₂₄, E₁₃, and E₁₄, with three of them being observed, matching previous reports^{16,26}. The *g*-factor of $|\pm 13/2\rangle$ along the *c*-axis is 3.3. The effective field exerted by the Er-Fe exchange interaction on the $|\pm 13/2\rangle$ states is also directly measured to be 0.13 THz at 10 K, which corresponds to the energy difference between E₁₃ and E₁₄, as shown in Fig. 2a. In addition, the broad peak around 2.04 THz is due to the transition from thermal populated $|\pm 13/2\rangle$ to $|\pm 11/2\rangle$ states.

The magnons and CFEs are strongly coupled in ErFeO₃, evidenced by the two avoided crossing regimes. The first one is between the qFM and the Er³⁺ EPR, accompanied by the enhancement of the Raman intensity of qFM at the high magnetic field branch. This observation is consistent with a previous THz absorption measurement, where Dicke cooperativity was observed⁵. The second one is between the qAFM and the CFE from $|-15/2\rangle$ to $|+13/2\rangle$. The enhanced Raman spectral weight of qAFM can be attributed to hybridization with CFE. We present the peak positions of magnons and CFEs at different magnetic fields in Fig. 2b. Phenomenologically, a 2×2 matrix can describe the coupling between magnon and CFE, with diagonal terms being uncoupled frequency and off-diagonals being coupling strength. The coupling strength is extracted to be 0.05 and 0.02 THz for qFM-EPR and qAFM-CFE couplings, respectively.

Besides coupled spin and orbital excitations, phonon-CFE strong coupling is also observed around 3.4 THz. The modes slightly affected by the magnetic field are optical phonons of ErFeO₃²³, referred to as P1 (3.3 THz), P2 (3.4 THz), and P3 (4.2 THz) hereinafter. Combining temperature-dependent and polarization-resolved Raman spectroscopy, we identify that the P1, P2, and P3 phonons carry B_{1g}, A_g, and A_g irreducible representations of point group *D*_{2h}, respectively, as

shown in Fig. 2c. The two modes with significant Zeeman shift correspond to the CFEs between the ground-state $|+15/2\rangle$ and the second excited state $|\pm 11/2\rangle$, labeled as E_{15} and E_{16} , as shown in Fig. 2d. The transition energy is consistent with previous absorption measurements¹⁶. Figure 3a presents the Zeeman splitting of crystal-field transitions from $|\pm 15/2\rangle$ to $|\pm 11/2\rangle$. The deviation from linearity at low magnetic fields results from the Er-Fe effective field. Besides a small g -factor of 0.1 along the c -axis, we find that $|\pm 11/2\rangle$ also exhibits the quadratic Zeeman effect, namely, the overall quadratic blueshift with increasing magnetic field⁵.

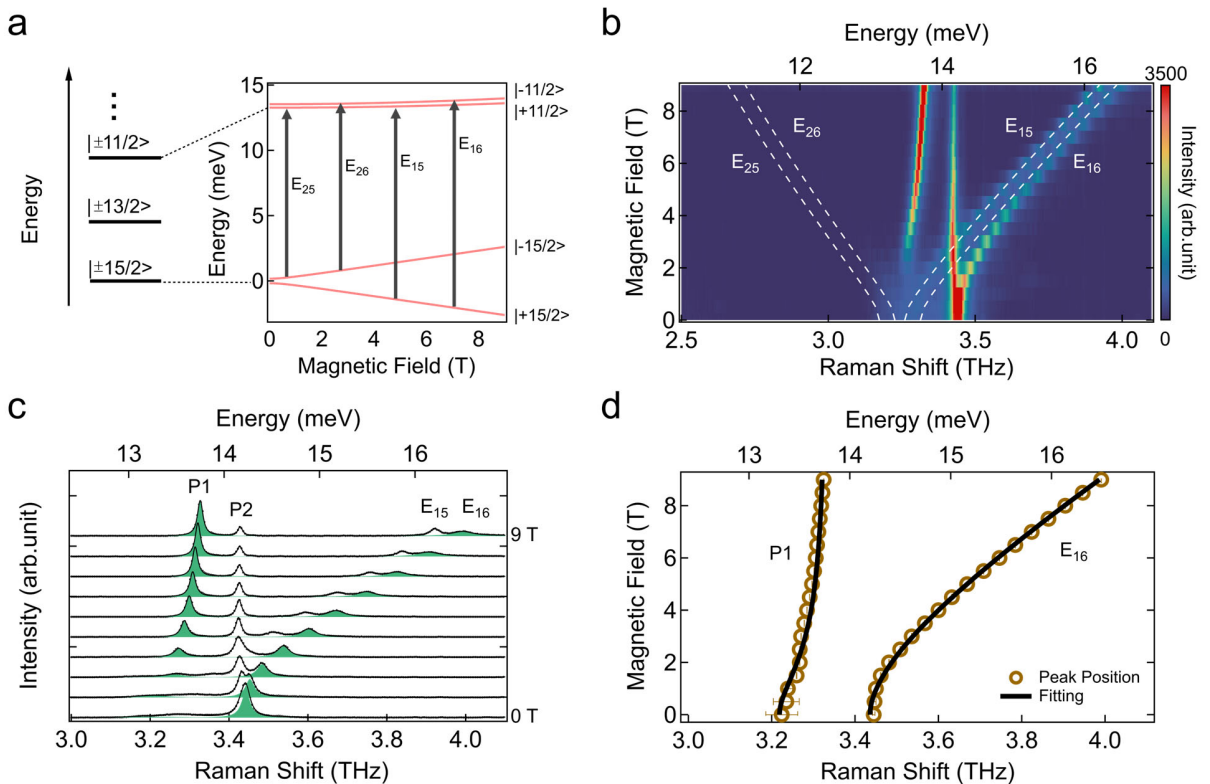


Figure 3 | Strongly coupled crystal-field excitation and P1 phonon at 10 K. **a**, schematic diagram of Zeeman-split crystal-field transitions from ground-state $|\pm 15/2\rangle$ to the second excited state $|\pm 11/2\rangle$, labeled as E_{25} , E_{26} , E_{15} , and E_{16} . **b**, comparison between uncoupled CFEs (white dotted lines) and the experimental data. **c**, Raman spectra of the phonon-CFE coupling region from 0 to 9 T. The green shaded peaks denote the modes that participate in the phonon-CFE coupling with Lorentz fitting. **d**, extracted peak positions of P1 and E_{16} in **c**. The fitting results are shown by black lines.

The strong coupling between phonons and CFEs opens a hybridization gap, manifested as a spectral avoided crossing. This feature is observed between P1 and E_{16} around 1 T. In contrast, E_{15} exhibits inconspicuous avoided crossing with P1. Instead, at high magnetic fields, E_{15} couples with

P3, as indicated by the increased spectral weight of E₁₅ and the slight blueshift of P3. From a symmetry perspective, the Kramers pair $|+11/2\rangle$ and $|{-11/2}\rangle$ carry different irreducible representations of the double point group C_s , meaning that the E₁₅ and E₁₆ should behave oppositely under the mirror operation. This explains why only P1-E₁₆ exhibits obvious coupling, while the P1-E₁₅ coupling is symmetry forbidden. Meanwhile, P2 is slightly affected by E₁₅ and E₁₆. Similar to the analysis of magnon-CFE coupling, we use a 2×2 matrix to model the coupling between P1 and E₁₆. The uncoupled frequencies of CFEs are depicted in Fig. 3b by white-dotted lines. Figure 3c presents the Lorentzian peak fitting of coupled phonon-CFE Raman spectra. The extracted eigenfrequencies are represented by black lines in Fig. 3d, yielding a coupling strength of 0.11 THz at 10 K. A detailed description of the fitting procedure and symmetry analysis is provided in the supporting information. In addition, since the E₁₆ transition arises from a non-degenerate ground-state multiplet of Er³⁺, the phonon-CFE strong coupling is closely linked to the pseudo JTE.

To investigate the cooperative scaling of the phonon-CFE coupling, we employ temperature variation as a pathway to control the effective population of coupled Jahn-Teller ions. At equilibrium, the occupation of each crystal-field state of Er³⁺ follows the Boltzmann distribution. Therefore, at given temperatures, the effective populations of Jahn-Teller ions can be obtained, which decrease as the temperature rises. Experimentally, the hybridization gap gradually shrinks with increasing temperature, and the phonon frequencies recover to their uncoupled values. The fitted eigenfrequencies of the coupling matrix are presented by white-dashed lines in Fig. 4a. To build the scaling relation, the coupling strength γ is plotted as a function of $\sqrt{\eta_{\text{CFE}}}$, with η_{CFE} representing the effective ground-state population (the number of coupled JT ions), defined as the difference in occupation probabilities between $|+15/2\rangle$ and $|{-11/2}\rangle$. Regarding the calculation of η_{CFE} , we take into account the Boltzmann distribution of the lowest eight Kramers energy levels of $^4\text{I}_{15/2}$ multiplet of the Er³⁺ ion, and calculate their occupation probabilities. Note that we also use ω_{phonon} to scale the $\sqrt{\eta_{\text{CFE}}}$ in the scaling equation, due to the avoided crossing gap being proportional to the phonon frequency⁵. More details can be found in the supplementary information. As shown in Fig. 4c, remarkably, a linear scaling relation holds for the coupling of P1-E₁₆, even at an elevated temperature of 90 K, a hallmark of Dicke-type cooperativity. The slight deviation of the linear scaling above 60 K could be attributed to the nonlinear coupling and

decoherent processes, such as thermal fluctuations and quasiparticle scattering. Due to the strong SOC dominating the electronic energy-level splitting in ErFeO_3 , we do not observe the structural phase transition stemming from the cooperative PJTE.

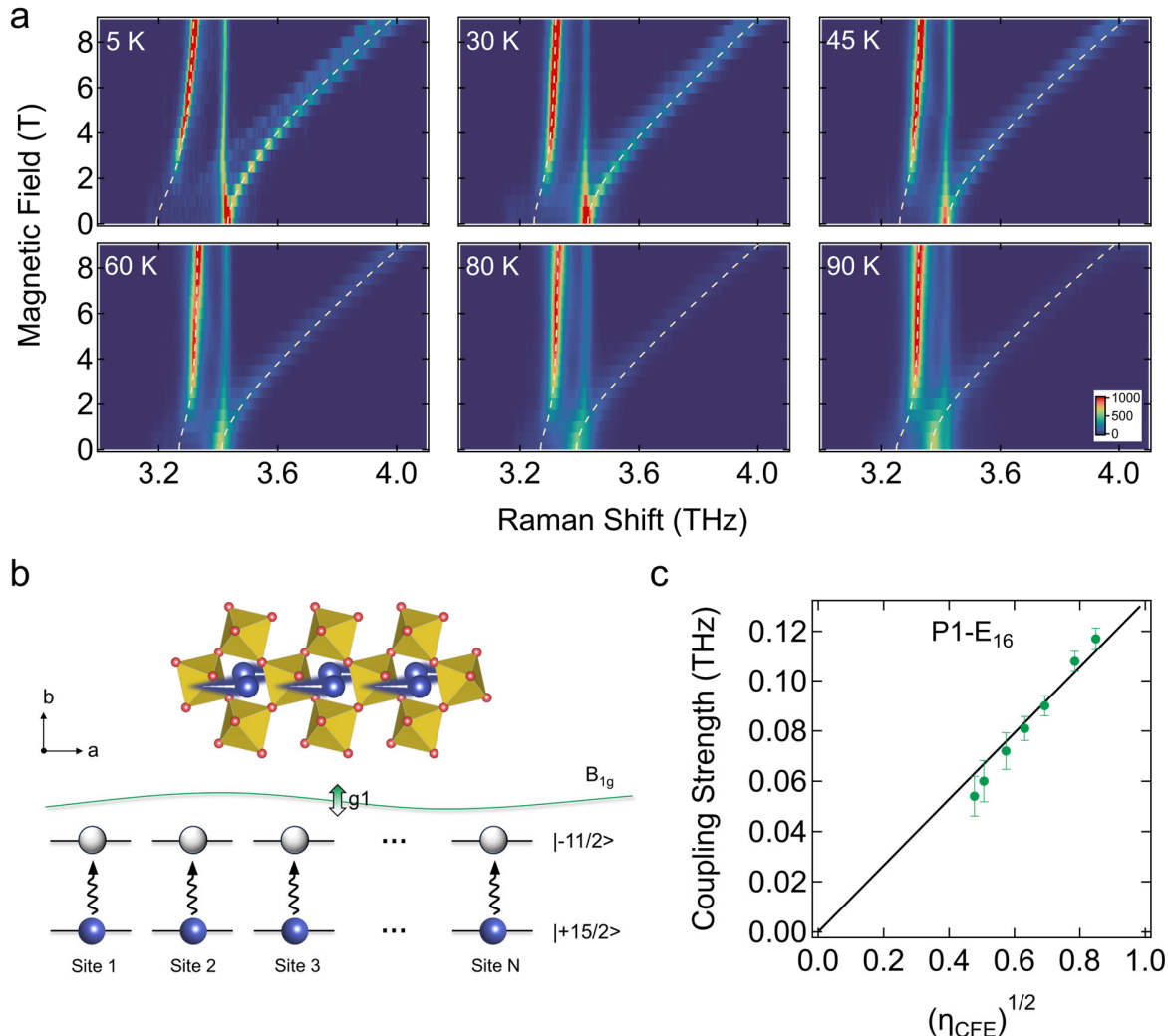


Figure 4 | Dicke cooperativity of phonon-CFE coupling in ErFeO_3 . **a**, the avoided crossing of the phonon-CFE coupling at different temperatures. The white dotted lines represent the fitting curves obtained by diagonalizing a 2×2 coupling matrix. **b**, schematic diagram illustrating the collective coupling of local Jahn-Teller ions to the long-range phonon (P1). The atomic motions are derived from density functional theory calculations, primarily corresponding to the vibration of Er^{3+} ions along the a -axis. **c**, the linear scaling relation between coupling strength and the square root of the effective ground-state population, corresponding to the temperatures at 5, 10, 30, 45, 60, 80, and 90 K.

Our experiments verify that the Dicke-type scaling relation can be extended to Jahn-Teller models, thereby establishing the phonon-CFE coupled system as a viable solid-state platform for

exploring Dicke physics²⁹. A promising direction is to investigate cooperative phenomena within a CFE-multimode phonons coupling system, which could serve as a solid quantum simulator for studying the multi-mode Dicke model in cavity quantum electrodynamics (cavity-QED)^{30,31}. Conversely, concepts developed within cavity-QED could offer new insight into long-standing problems related to Jahn-Teller distortions, such as guiding the control of superconductivity and colossal magnetoresistance in perovskite-type oxides by tailoring (pseudo-) JTE strength³²⁻³⁶, potentially through population control as demonstrated above. Furthermore, our spectroscopy results reveal the magnon-CFE and phonon-CFE hybridizations in ErFeO₃, clearly indicating the strongly coupled spin, orbital, and lattice degrees of freedom in this system. The cooperative phonon-CFE coupling provides unique opportunities to explore ultrafast THz spin dynamics through phonon-modulated magnetic anisotropy. Previous work has shown that driving specific phonons in ErFeO₃ can transiently excite qAFM modes¹⁷. We speculate that the modulation of magnetic anisotropy by the P1 phonon may also contribute to the excitation of coherent magnons.

Reference

- 1 Bersuker, I. B. Pseudo-Jahn-teller effect-a two-state paradigm in formation, deformation, and transformation of molecular systems and solids. *Chem. Rev.* **113**, 1351-1390 (2013). <https://doi.org/10.1021/cr300279n>
- 2 Dicke, R. H. Coherence in spontaneous radiation processes. *Phys. Rev.* **93**, 99-110 (1954). <https://doi.org/10.1103/PhysRev.93.99>
- 3 Hepp, K. & Lieb, E. H. On the superradiant phase transition for molecules in a quantized radiation field: the Dicke maser model. *Ann. Phys.* **76**, 360-404 (1973). [https://doi.org/10.1016/0003-4916\(73\)90039-0](https://doi.org/10.1016/0003-4916(73)90039-0)
- 4 Tavis, M. & Cummings, F. W. Approximate solutions for an N-molecule-radiation-field Hamiltonian. *Phys. Rev.* **188**, 692-695 (1969). <https://doi.org/10.1103/PhysRev.188.692>
- 5 Li, X. *et al.* Observation of Dicke cooperativity in magnetic interactions. *Science* **361**, 794-797 (2018). <https://doi.org/10.1126/science.aat5162>
- 6 Baumann, K., Guerlin, C., Brennecke, F. & Esslinger, T. Dicke quantum phase transition with a superfluid gas in an optical cavity. *Nature* **464**, 1301-1306 (2010). <https://doi.org/10.1038/nature09009>
- 7 Zhang, X. *et al.* Observation of a superradiant quantum phase transition in an intracavity degenerate Fermi gas. *Science* **373**, 1359-1362 (2021). <https://doi.org/10.1126/science.abd4385>
- 8 Hioe, F. T. Phase transitions in some generalized Dicke models of superradiance. *Phys. Rev. A* **8**, 1440-1445 (1973). <https://doi.org/10.1103/PhysRevA.8.1440>
- 9 Han, Y., Li, H. & Yi, W. Interaction-enhanced superradiance of a Rydberg-atom array. *Phys. Rev. Lett.* **133** (2024). <https://doi.org/10.1103/PhysRevLett.133.243401>

10 Bamba, M., Li, X., Marquez Peraca, N. & Kono, J. Magnonic superradiant phase transition. *Commun. Phys.* **5** (2022). <https://doi.org/10.1038/s42005-021-00785-z>

11 Marquez Peraca, N. *et al.* Quantum simulation of an extended Dicke model with a magnetic solid. *Commun. Mater.* **5** (2024). <https://doi.org/10.1038/s43246-024-00479-3>

12 Kim, D. *et al.* Observation of the magnonic Dicke superradiant phase transition. *Sci. Adv.* **11**, ead1691 (2025). <https://doi.org/10.1126/sciadv.adt1691>

13 Gehring, G. A. & Gehring, K. A. Co-operative Jahn-Teller effects. *Rep. Prog. Phys.* **38**, 1-89 (1975). <https://doi.org/10.1088/0034-4885/38/1/001>

14 Majerníková, E. & Shpyrko, S. Quantum phase crossover and chaos in a generalized Jahn-Teller lattice model. *Journal of Physics A: Mathematical and Theoretical* **44** (2011). <https://doi.org/10.1088/1751-8113/44/6/065101>

15 Bersuker, I. B. *The Jahn-Teller Effect*. (Cambridge University Press, 2006).

16 Wood, D. L., Holmes, L. M. & Remeika, J. P. Exchange fields and optical Zeeman effect in ErFeO₃. *Phys. Rev.* **185**, 689-695 (1969). <https://doi.org/10.1103/PhysRev.185.689>

17 Nova, T. F. *et al.* An effective magnetic field from optically driven phonons. *Nat. Phys.* **13**, 132-136 (2017). <https://doi.org/10.1038/nphys3925>

18 Hougen, J. T. & Singh, S. Electronic Raman effect in Pr³⁺ ions in single crystals of PrCl₃. *Phys. Rev. Lett.* **10**, 406-407 (1963). <https://doi.org/10.1103/PhysRevLett.10.406>

19 Axe, J. D. Two-photon processes in complex atoms. *Phys. Rev.* **136**, A42-A45 (1964). <https://doi.org/10.1103/PhysRev.136.A42>

20 Mortensen, O. S. & Koningstein, J. A. Electronic Raman effect. II. Asymmetry of the scattering tensor for electronic Raman transitions. *J. Chem. Phys.* **48**, 3971-3977 (1968). <https://doi.org/10.1063/1.1669722>

21 Fleury, P. A. & Loudon, R. Scattering of light by one- and two-magnon excitations. *Phys. Rev.* **166**, 514-530 (1968). <https://doi.org/10.1103/PhysRev.166.514>

22 Shapiro, S. M., Axe, J. D. & Remeika, J. P. Neutron-scattering studies of spin waves in rare-earth orthoferrites. *Phys. Rev. B* **10**, 2014-2021 (1974). <https://doi.org/10.1103/PhysRevB.10.2014>

23 Koshizuka, N. & Ushioda, S. Inelastic-light-scattering study of magnon softening in ErFeO₃. *Phys. Rev. B* **22**, 5394-5399 (1980). <https://doi.org/10.1103/PhysRevB.22.5394>

24 Yamaguchi, T. Theory of spin reorientation in rare-earth orthochromites and orthoferrites. *J Phys Chem Solids* **35**, 479-500 (1974). [https://doi.org/10.1016/S0022-3697\(74\)80003-X](https://doi.org/10.1016/S0022-3697(74)80003-X)

25 Mukhin, A. A. *et al.* Submillimeter and far IR spectroscopy of magneto- and electrodipolar rare-earth modes in the orthoferrite TmFeO₃. *Phys. Lett. A* **153**, 499-504 (1991). [https://doi.org/10.1016/0375-9601\(91\)90705-d](https://doi.org/10.1016/0375-9601(91)90705-d)

26 Mikhaylovskiy, R. V., Huisman, T. J., Pisarev, R. V., Rasing, T. & Kimel, A. V. Selective excitation of terahertz magnetic and electric dipoles in Er³⁺ Ions by femtosecond laser pulses in ErFeO₃. *Phys. Rev. Lett.* **118**, 017205 (2017). <https://doi.org/10.1103/PhysRevLett.118.017205>

27 Kimel, A. V. & Zvezdin, A. K. Universal orthoferrites and orthoferrites as a universe. *Photonics Insights* **1** (2022). <https://doi.org/10.3788/pi.2022.C03>

28 Li, X., Kim, D., Liu, Y. & Kono, J. Terahertz spin dynamics in rare-earth orthoferrites. *Photonics Insights* **1** (2022). <https://doi.org/10.3788/pi.2022.R05>

29 Larson, J. Jahn-Teller systems from a cavity QED perspective. *Phys. Rev. A* **78** (2008). <https://doi.org/10.1103/PhysRevA.78.033833>

30 Tolkunov, D. & Solenov, D. Quantum phase transition in the multimode Dicke model. *Phys. Rev. B* **75** (2007). <https://doi.org/10.1103/PhysRevB.75.024402>

31 Fiorelli, E., Marcuzzi, M., Rotondo, P., Carollo, F. & Lesanovsky, I. Signatures of associative memory behavior in a multimode Dicke model. *Phys. Rev. Lett.* **125**, 070604 (2020). <https://doi.org/10.1103/PhysRevLett.125.070604>

32 Bersuker, I. B. On the origin of ferroelectricity in perovskite-type crystals. *Phys. Lett.* **20**, 589-590 (1966). [https://doi.org/10.1016/0031-9163\(66\)91127-9](https://doi.org/10.1016/0031-9163(66)91127-9)

33 Millis, A. J., Littlewood, P. B. & Shraiman, B. I. Double exchange alone does not explain the resistivity of $\text{La}_{1-x}\text{Sr}_x\text{MnO}_3$. *Phys. Rev. Lett.* **74**, 5144-5147 (1995). <https://doi.org/10.1103/PhysRevLett.74.5144>

34 Tokura, Y. & Nagaosa, N. Orbital physics in transition-metal oxides. *Science* **288**, 462-468 (2000). <https://doi.org/10.1126/science.288.5465.462>

35 Bednorz, J. G. & Müller, K. A. Perovskite-type oxides—The new approach to high- T_c superconductivity. *Rev. Mod. Phys.* **60**, 585-600 (1988). <https://doi.org/10.1103/RevModPhys.60.585>

36 Millis, A. J. Cooperative Jahn-Teller effect and electron-phonon coupling in $\text{La}_{1-x}\text{A}_x\text{MnO}_3$. *Phys. Rev. B* **53**, 8434-8441 (1996). <https://doi.org/10.1103/physrevb.53.8434>

37 Kresse, G. & Furthmüller, J. Efficient iterative schemes for ab initio total-energy calculations using a plane-wave basis set. *Phys. Rev. B* **54**, 11169-11186 (1996). <https://doi.org/10.1103/physrevb.54.11169>

38 Perdew, J. P. *et al.* Restoring the density-gradient expansion for exchange in solids and surfaces. *Phys. Rev. Lett.* **100**, 136406 (2008). <https://doi.org/10.1103/PhysRevLett.100.136406>

39 Blochl, P. E. Projector augmented-wave method. *Phys. Rev. B* **50**, 17953-17979 (1994). <https://doi.org/10.1103/physrevb.50.17953>

40 Togo, A. & Tanaka, I. First principles phonon calculations in materials science. *Scr. Mater.* **108**, 1-5 (2015). <https://doi.org/10.1016/j.scriptamat.2015.07.021>

Methods:

Single crystal growth and sample preparation: High-purity Er_2O_3 (99.99%) and Fe_2O_3 (99.98%) powders were weighed in a stoichiometric ratio, ground in ethanol, and calcined at 1250 °C for 1000 minutes. The polycrystalline powder was reground, pressed into thin disks (~1.5 mm thick), and sintered again under the same conditions. After a third grinding, the powder was compacted into rods (40–85 mm long, 5–6 mm in diameter) at 70 MPa and sintered at 1250 °C. A high-quality ErFeO_3 single crystal was grown using an optical floating zone furnace with opposite rod rotation (15 rpm) and a growth rate of 3 mm/h. The crystallographic orientation of the as-grown ErFeO_3 single crystal was determined using back-reflection Laue X-ray diffraction. The presence of well-defined and sharp Laue spots confirmed the high crystalline quality. Subsequently, three oriented single-crystal plates, each perpendicular to the a -, b -, and c -axes, were carefully cut from the bulk crystal.

Magneto-Raman measurement: A He-Ne laser (633 nm) was used to excite the c -cut ErFeO_3 sample, which was placed in a closed-cycle cryostat (attoDRY 2100) with a magnetic field up to 9 T applied in Faraday geometry. The Raman signal went through Bragg notch filters and was detected by a high-resolution spectrometer with a liquid nitrogen-cooled CCD camera. The temperature-dependent Raman spectra were acquired with a depolarization configuration. A zero-order half-wave plate was employed in polarization-resolved Raman spectroscopy. The spectral resolution is 0.004 THz.

The first-principles calculation: All density functional theory (DFT) calculations were performed with the Vienna Ab initio Simulation Package (VASP)³⁷, where the Perdew-Burke-Ernzerhof functional modified for solids (PBEsol) within the generalized gradient approximation was chosen as the exchange-correlation functional³⁸. The projector augmented-wave method was used with the energy cutoff of 800 eV, together with a k -mesh spacing of $6 \times 6 \times 4$ ³⁹. In structural optimization, we implemented DFT+U to correct the Fe 3d states, where $U = 3.7$ eV and $J = 0.7$ eV. The convergence criteria were set as 1×10^{-3} eV/Å and 1×10^{-6} eV for force and energy per atom, respectively. The phonon spectrum was calculated using the PHONOPY package with the finite displacement method⁴⁰. A $2 \times 2 \times 2$ supercell was used in the phonon calculation.

Acknowledgements: We thank Xinwei Li for valuable discussions. This work was supported by the National Key Research and Development Program of China (Grants No. 2020YFA0309200, 2021YFA1403800, 2024YFA1408700), the National Natural Science Foundation of China (Grants No. 12474475, 12374116, 12125404, T2495231, 12250008, 12188101), the Natural Science Foundation of Jiangsu Province (Grants No. BK20240057, BK20243011, and BK20233001), the Fundamental Research Funds for the Central Universities, the CAS project for Young Scientists in Basic Research (Grant No. YSBR-059), the fellowship from the China Postdoctoral Science Foundation (Grants No. 2024M751931, 2025M773408 and GZB20250786), the Jiangsu Funding Program for Excellent Postdoctoral Talent (Grants No. 2025ZB376). M. B. is supported by the Research Foundation for Opto-Science and Technology, and the Japan Society for the Promotion of Science (JSPS) (Grant No. JPJSJRP20221202 and KAKENHI Grants No. JP24K21526, JP25K00012, JP25K01691, and JP25K01694).

Author contributions: F.W. performed optical measurements and data analysis under the supervision of Q.Z. X.M. and S.C. synthesized and characterized the samples. Z.Z. and J.S. carried out the first-principles calculation. M.B. and Y.W. contributed to the data interpretation. F.W. and Q.Z. wrote the paper with input from all authors.

Competing Interests: The authors declare no competing financial interests.

Data Availability: The datasets generated during and/or analyzed during this study are available from the corresponding author upon reasonable request.